Production of π^0 and η mesons at large transverse momenta in $\pi^- p$ and π^-Be interactions at 515 GeV/c

L. Apanasevich,[1,2] J. Bacigalupi,[3] W. Baker,[4] M. Begel,[2] S. Blusk,[5] C. Bromberg,[1] P. Chang,[6] B. Choudhary,[7] W. H. Chung,[5] L. de Barbaro,[2] W. DeSoi,[2] W. Długosz,[6] J. Dunlea,[2] E. Engels, Jr.,[5] G. Fanourakis,[2] T. Ferbel,[2] J. Ftacnik,[2] D. Garelick,[6] G. Ginther,[2] M. Glaubman,[6] P. Gutierrez,[8] K. Hartman,[9] J. Huston,[1] C. Johnstone,[4] V. Kapoor,[7] J. Kuehler,[8] C. Lirakis,[6] F. Lobkowicz,[2,*] P. Lukens,[4] J. Mansour,[2] A. Maul,[1] R. Miller,[1] B. Y. Oh,[9] G. Osborne,[2] D. Pellett,[3] E. Prebys,[2] R. Roser,[2] P. Shepard,[5] R. Shivpuri,[7] D. Skow,[4] P. Slattery,[2] L. Sorrell,[1] D. Striley,[6] W. Toothacker,[9,*] S. M. Tripathi,[3] N. Varelas,[2] D. Weerasundara,[5] J. J. Whitmore,[9] T. Yasuda,[6] C. Yosef,[1] M. Zieliński,[2] and V. Zutshi[7]

[1]*Michigan State University, East Lansing, Michigan 48824, USA*
[2]*University of Rochester, Rochester, New York 14627, USA*
[3]*University of California-Davis, Davis, California 95616, USA*
[4]*Fermi National Accelerator Laboratory, Batavia, Illinois 60510, USA*
[5]*University of Pittsburgh, Pittsburgh, Pennsylvania 15260, USA*
[6]*Northeastern University, Boston, Massachusetts 02115, USA*
[7]*University of Delhi, Delhi, India 110007*
[8]*University of Oklahoma, Norman, Oklahoma 73019, USA*
[9]*Pennsylvania State University, University Park, Pennsylvania 16802, USA*

(Fermilab E706 Collaboration)

(Received 11 August 2003; published 26 February 2004)

We present results on the production of high transverse momentum π^0 and η mesons in $\pi^- p$ and π^-Be interactions at 515 GeV/c. The data span the kinematic ranges $1 < p_T < 11$ GeV/c in transverse momentum and $-0.75 \leqslant y_{\rm cm} \leqslant 0.75$ in rapidity. The inclusive π^0 cross sections are compared with next-to-leading order QCD calculations and to expectations based on a phenomenological parton-k_T model.

DOI: 10.1103/PhysRevD.69.032003 PACS number(s): 12.38.Qk, 13.85.Ni

I. INTRODUCTION

The study of inclusive single-hadron production at large transverse momentum (p_T) has been a useful probe in the development of perturbative QCD (PQCD) [1,2]. Early in the evolution of the parton model, a departure from an exponential dependence of particle production at low p_T was interpreted in terms of the onset of interactions between point-like constituents (partons) contained in hadrons. Large p_T is a regime where perturbative methods have been applied to QCD to provide quantitative comparisons with data. Such comparisons yield information on the validity of the PQCD description, and on the parton distribution functions of hadrons and the fragmentation functions of partons.

This paper reports high-precision measurements of the production of π^0 and η mesons with large p_T by a 515 GeV/c π^- beam. The data were accumulated during the 1990 and 1991–1992 fixed-target runs at Fermilab. The π^0 production cross sections are compared with next-to-leading order (NLO) PQCD calculations [3]. As illustrated in a previous publication [4], our data for both inclusive π^0 and direct-photon production are not described satisfactorily by the available NLO PQCD calculations using standard choices of parameters. Similar discrepancies have been observed [5,6] between conventional PQCD calculations and other measurements of high-p_T π^0 and direct-photon cross sections (see also [7–9]). The origin of these discrepancies can be attributed to the effects of initial-state soft-gluon radiation. Such radiation generates transverse components of initial-state parton momenta, referred to below as k_T [10]. Evidence of significant k_T in various processes and a phenomenological model for incorporating its effect on the calculated high-p_T cross sections has been extensively discussed in Refs. [4], [5]. Recent studies of the photoproduction of direct photons at the DESY ep collider at HERA may provide additional insight [11–15]. In this paper, we follow the phenomenological prescription of Ref. [5] when comparing calculations with our π^0 data.

II. EXPERIMENTAL APPARATUS

A. Spectrometer

Fermilab E706 was a fixed-target experiment designed to measure the production of direct photons, neutral mesons, and associated particles at high p_T [4,16–18]. The spectrometer, designed and built for this experiment, was located in the Meson West experimental hall and included a precision charged particle tracking system and a large acceptance liquid argon calorimeter. Figure 1 shows key elements of the Meson West spectrometer [19].

The tracking system consisted of silicon microstrip detectors (SSDs) in the target region, and multiwire proportional chambers (PWCs) and straw tube drift chambers (STDCs) downstream of a large aperture analysis magnet [18]. The SSD system contained 16 planes of silicon wafers, arranged in 8 modules. Each module contained two SSD planes, one providing X-view information and the other providing

*Deceased.

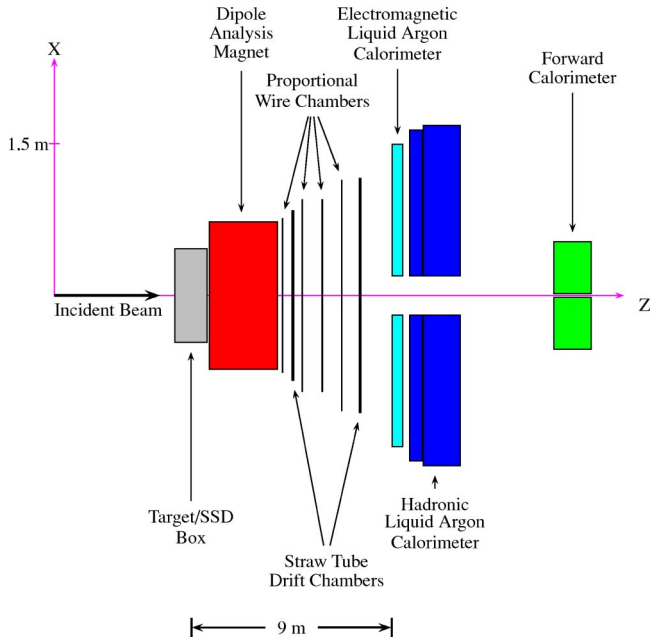

FIG. 1. Plan view of the Meson West spectrometer (omitting muon identification). The *Z* axis of the coordinate system for the experiment was oriented along the nominal beam axis.

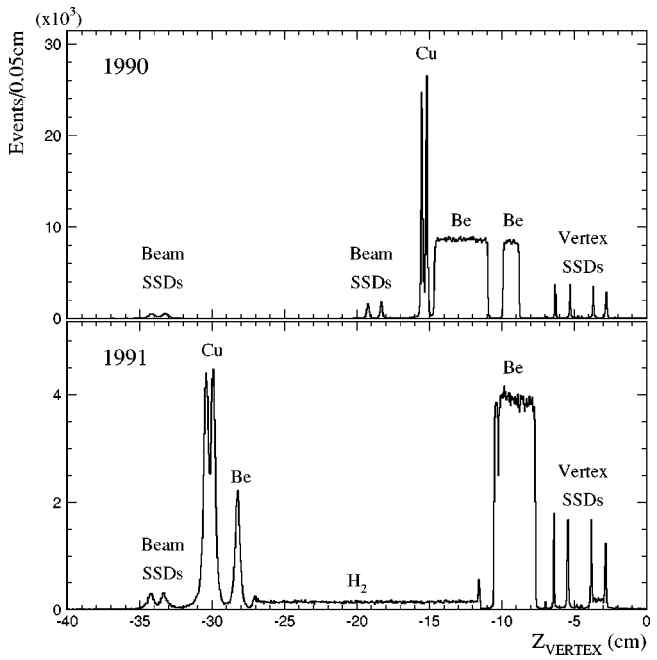

FIG. 2. The longitudinal distribution of reconstructed vertices for the 1990 (top) and 1991–1992 (bottom) target configurations.

Y-view information. Six 3×3 cm^2 SSD planes were located upstream of the target and used to reconstruct beam tracks. Two hybrid 5×5 cm^2 SSD planes (25 μm pitch strips in the central 1 cm, 50 μm beyond) were located downstream of the target. These were followed by eight 5×5 cm^2 SSD planes of 50 μm pitch. The analysis dipole imparted a transverse momentum impulse in the horizontal plane of $\approx$450 MeV/c to charged particles. Downstream track segments were measured by means of four stations of four views ($XYUV$) of 2.54 mm pitch PWCs and two stations of eight ($4X4Y$) layers of STDCs with tube diameters 1.04 cm (upstream station) and 1.63 cm (downstream station).

In the 1990 run, the target consisted of two 0.8-mm-thick copper foils followed by two pieces of beryllium. The upstream Be piece was 3.7 cm long, while the downstream Be piece was 1.1 cm long. For the 1991–1992 run, the target was reconfigured to include a liquid hydrogen target [20] contained in a 15.3-cm-long Mylar flask and supported in an evacuated volume with beryllium windows at each end (2.5 mm thickness upstream and 2.8 mm thickness downstream). The liquid hydrogen target was flanked by two 0.8-mm-thick copper disks upstream and a 2.54-cm-long beryllium cylinder downstream. Figure 2 shows the reconstructed vertex position along *Z* as determined by the tracking system for representative samples from the 1990 (top) and 1991–1992 (bottom) runs. The individual target elements are clearly resolved, as are several of the SSDs.

Photons were detected in a large, lead and liquid-argon sampling electromagnetic calorimeter (EMLAC), located 9 m downstream of the target [21]. The EMLAC had a cylindrical geometry with an inner radius of 20 cm and an outer radius of 160 cm. It was divided into four mechanically independent quadrants, which were further subdivided electronically to create octants. The calorimeter had 33 longitudinal cells, read out in two sections: an 11 cell front section ($\approx$8.5 radiation lengths) and a 22 cell back section ($\approx$18 radiation lengths). The longitudinal cells consisted of 2-mm-thick lead cathodes (the first cathode was constructed of aluminum), double-sided copper-clad G-10 radial (R) anode boards followed by 2-mm-thick lead cathodes, and double-sided copper-clad G-10 azimuthal (Φ) anode boards. There were 2.5 mm argon gaps between each of these layers in a cell. The copper cladding on the anode boards was cut to form strips. Signals from corresponding strips on all R (or Φ) anode boards in the front (or back) section were jumpered together. The copper cladding on the radial anode boards was cut into concentric strips centered on the nominal beam axis. The width of the strips on the first R board was 5.5 mm. The width of the R strips on the following R boards increased slightly so that the radial geometry was projective relative to the target. The azimuthal readout was subdivided at a radius of 40 cm into inner and outer segments, with each inner Φ strip subtending an azimuthal angle of $\pi/192$ radians and outer Φ strips covering $\pi/384$ radians. Subdivision of the azimuthal strips in the outer portion of the detector improved both the position and energy resolution for showers reconstructed in this region. It also reduced R-Φ correlation ambiguities from multiple showers in the same octant of the calorimeter.

The spectrometer also included two other calorimeters: a hadronic calorimeter located downstream of the EMLAC within the same cryostat and a steel and scintillator calorimeter positioned further downstream to provide instrumentation in the very forward region. The E672 muon spectrometer, consisting of a toroidal magnet, scintillators, and proportional wire chambers, was deployed immediately downstream of the calorimeters [22–25].

The beamline was instrumented with a differential Cherenkov counter [26,27] to identify incident pions, kaons, and protons in secondary beams. This helium-filled counter was 43.4 m long and was located ≈100 m upstream of the experiment's target. At the end of the beamline was a 4.7-m-long stack of steel surrounding the beam pipe and shadowing the EMLAC to absorb off-axis hadrons. A water tank was placed at the downstream end of this hadron shield to absorb low-energy neutrons. Surrounding the hadron shield and neutron absorber were walls of scintillation counters (VW) to identify penetrating muons. During the 1990 run, there was one wall at the upstream end and two walls at the downstream end of the hadron absorber. Prior to the 1991–1992 run, an additional wall was added to the upstream end.

B. Trigger

The E706 trigger selected events yielding high transverse momentum showers in the EMLAC. The selection process involved several stages: beam and interaction definitions and pretrigger and high-p_T trigger requirements. Beam particles were detected using a hodoscope consisting of three planes (arranged in *X*, *Y*, and *U* views) of scintillator strips, located ≈2 m upstream of the target region. A BEAM signal was generated if the beam hodoscope registered hits in time coincidence from at least two of the three planes. In addition, a BEAM1 signal was generated if the hits in at least two of the hodoscope planes were considered to be isolated. Scintillation counters centered on the target with a 0.95-cm-diameter central hole were used to reject interactions initiated by particles in the beam halo.

Interactions were detected using two pairs of scintillation counters mounted on the dipole analysis magnet, one pair on the upstream side and one pair downstream. Each pair had a central hole that allowed non-interacting beam particles to pass through undetected. An INTERACTION was defined as a coincidence between signals from at least two of these four interaction counters. A filter was used to reject interactions that occurred within 60 ns of one another to minimize potential confusion in the EMLAC due to out-of-time interactions.

For those interactions that satisfied both the BEAM1 and INTERACTION definitions, the p_T deposited in various regions of the EMLAC was evaluated by weighting the energy signals from the fast outputs of the EMLAC *R* channel amplifiers by a factor proportional to $\sin\theta_i$, where θ_i is the polar angle that the *i*th strip subtended with respect to the nominal beam axis. The PRETRIGGER HI signal required that the p_T detected in either the inner or outer *R* channels of any octant be greater than the pretrigger threshold value. This signal was issued only when there was no evidence in that octant of substantial noise or significant p_T attributable to an earlier interaction, and there was no incident beam halo muon detected by the VW.

Localized trigger groups were formed for each octant by clustering the inputs from the *R* channels into 32 groups of 8 channels. Each of the adjacent pairs of 8 channel groups formed a group of 16 strips. If the p_T detected in any of these groups of 16 was above a specified high (or low) threshold, then a LOCAL HI (or LOCAL LO) signal was generated for that octant. If a LOCAL HI (or LOCAL LO) signal was generated in coincidence with the PRETRIGGER HI in the same octant, then a SINGLE LOCAL HI (or SINGLE LOCAL LO) trigger was generated for that octant.

Trigger decisions were also made based upon global energy depositions in an octant. A GLOBAL LO signal was generated if the total p_T in an octant exceeded a low global threshold value. The LOCAL⊗GLOBAL LO trigger required a coincidence of the GLOBAL LO signal with PRETRIGGER HI and LOCAL LO signals from the same octant. The LOCAL LO requirement was included to suppress spurious global triggers due to coherent noise in the EMLAC.

The SINGLE LOCAL LO and LOCAL⊗GLOBAL LO triggers were prescaled to keep them from dominating the data sample. Prescaled samples of beam, interaction, and pretrigger events were also recorded. Further details concerning the E706 trigger can be found elsewhere [16,18,28,29].

III. ANALYSIS METHODS

This paper presents results for π^0 and η production by a 515 GeV/*c* π^- beam on beryllium and liquid hydrogen targets. The data sample used in this analysis corresponds to an integrated luminosity of 7.5 pb^{-1} of π^-Be data (6.1 pb^{-1} from the 1990 run plus 1.4 pb^{-1} from the 1991–1992 run) and 0.23 pb^{-1} of $\pi^- p$ data. The following subsections describe the data analysis procedures and the methods used to correct the data for losses due to inefficiencies and selection biases. Additional details may be found in several of our previous papers [16,18,21].

A. Reconstruction

Two major aspects of the event reconstruction procedure were particle track and calorimeter shower reconstruction. The charged-track reconstruction algorithm produced track segments upstream of the magnet using information from the SSDs, and downstream of the magnet using information from the PWCs and STDCs. These track segments were projected to the center of the magnet and linked to form the final reconstructed tracks, whose calculated charges and momenta were used in physics analyses and to determine the location of the primary interaction vertex. The charged track reconstruction is described in detail in Ref. [18].

The readout in each EMLAC quadrant consisted of four regions: left *R* and right *R* (radial strips of each octant in that quadrant) and inner Φ and outer Φ. The distributions of energy from clusters of strips in each region were fit to the shape of an electromagnetic shower as determined from Monte Carlo simulations and isolated-shower data. These fits were used to evaluate the positions and energies of the peaks in each region. Peaks of approximately the same energy in the *R* and Φ regions within the same half octant were combined to obtain the final shower positions and energies (more complex algorithms were used to handle configurations with overlapping showers in either the *R* or Φ region). The EMLAC readout was also subdivided longitudinally into front and back sections. This longitudinal segmentation provided discrimination between showers generated by electromagnetically or hadronically interacting particles. An expanded

discussion of the EMLAC reconstruction procedures and performance can be found in Ref. [21].

B. Event selection and meson signals

Events contributing to measurements of cross sections were required to have reconstructed interactions vertices within the fiducial volume of the Be or H_2 targets. Both π^0 and η mesons were reconstructed via their $\gamma\gamma$ decay modes. Only those showers which deposited at least 20% of their energy in the front part of EMLAC were considered as γ candidates, to reduce the background due to showers from hadronic interactions. Only those $\gamma\gamma$ combinations with energy asymmetry $A_{\gamma\gamma} \equiv |E_{\gamma 1} - E_{\gamma 2}|/(E_{\gamma 1} + E_{\gamma 2}) < 0.75$ were considered in order to reduce uncertainties due to low energy photons. Photons were required to be reconstructed within the fiducial region of the EMLAC to exclude areas with reduced sensitivity. In particular, regions of the detector near quadrant boundaries (which abutted steel support plates), the central beam hole, the outer radius of the EMLAC, and octant boundaries were excluded. In addition, $\gamma\gamma$ combinations were restricted to the same octant to simplify the trigger analysis. A simple ray-tracing Monte Carlo program was employed to determine the correction for these fiducial requirements.

Signals have been corrected for the 25% loss due to the energy asymmetry cut and for the branching fractions for the $\gamma\gamma$ decay modes [30]. The correction for losses due to the conversion of one or both of the photons into e^+e^- pairs was evaluated by projecting each reconstructed photon from the event vertex to the reconstructed position in the EMLAC. The radiation length of material traversed was calculated based upon detailed descriptions of the detectors encountered. The photon conversion probability was evaluated and used to account for conversion losses. The average correction for conversion losses per meson was 1.19 for the Be target in the 1990 run (1.16 in 1991–1992) and 1.24 for the H_2 target. A full event simulation (described below) was employed to correct for other effects including reconstruction smearing and losses.

The $\gamma\gamma$ invariant mass distributions in the π^0 and η mass regions for photon pairs that satisfied the above requirements are shown in Figs. 3 and 4 for several $\gamma\gamma$ p_T intervals. A π^0 candidate was defined as a combination of two photons with invariant mass, $M_{\gamma\gamma}$, in the range $100\ \mathrm{MeV}/c^2 < M_{\gamma\gamma} < 180\ \mathrm{MeV}/c^2$. An η candidate was defined as a two-photon combination in the range $450\ \mathrm{MeV}/c^2 < M_{\gamma\gamma} < 650\ \mathrm{MeV}/c^2$. Combinatorial background under the π^0 and η peak regions was evaluated as follows. Sideband regions were defined to cover a mass range equivalent to that in the π^0 and η peak regions. Distributions from these sidebands were subtracted from the distributions within the π^0 and η mass ranges to obtain the respective signals. This technique is appropriate as long as the combinatorial background depends approximately linearly on $M_{\gamma\gamma}$. The combinatorial background shape is not linear at low p_T (below $\approx 2\ \mathrm{GeV}/c$), and a fitting procedure was used to evaluate this background. The $\gamma\gamma$ mass distributions at low p_T were fit using Gaussians for signal, and second and third order polynomials for the background. The combinatorial background in the peak regions was determined from the resultant fit parameters, and subsequently subtracted from the total entries within the peak.

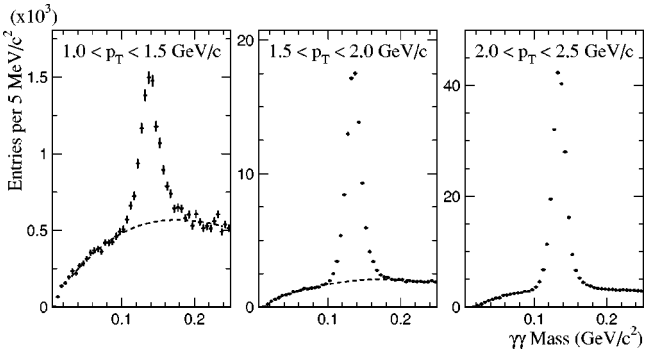

FIG. 3. $\gamma\gamma$ mass distributions in the region of the π^0 for several p_T bins. Curves are overlayed for those p_T bins where the background to the signal was determined using a fitting procedure rather than sideband subtraction.

C. Trigger corrections

Trigger corrections were evaluated on an event-by-event basis using the measured efficiencies of the trigger groups responsible for the formation of a given trigger. For example, the SINGLE LOCAL HI trigger corrections were based upon the efficiencies of the 32 groups of 16 in the triggering octant. These efficiencies were evaluated as functions of the p_T reconstructed within the trigger group, using data samples that were unbiased with respect to the trigger group. From these efficiencies, a trigger probability was defined, $P = 1 - \Pi(1 - p_i)$, where p_i is the efficiency of the ith trigger group in the octant. The inverse of this probability was applied as a trigger weight to each meson candidate. Meson candidates with trigger probabilities of $P < 0.1$ were excluded from further consideration to avoid excessively large trigger weights. The correction for losses from this requirement was determined from Monte Carlo, and absorbed into the reconstruction efficiency.

The cross sections presented in this paper utilize the results from a combination of triggers. Going from low to high p_T, the triggers were INTERACTION, PRETRIGGER HI,

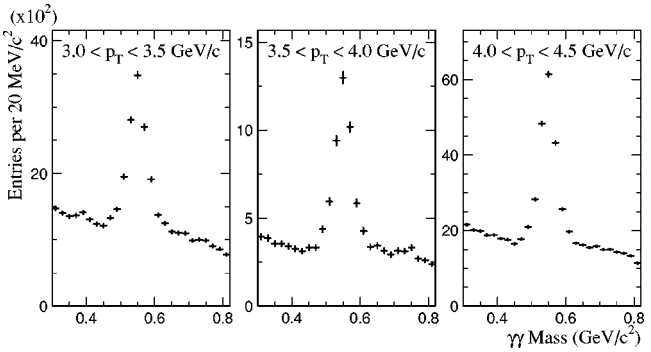

FIG. 4. $\gamma\gamma$ mass distributions in the region of the η for several p_T bins.

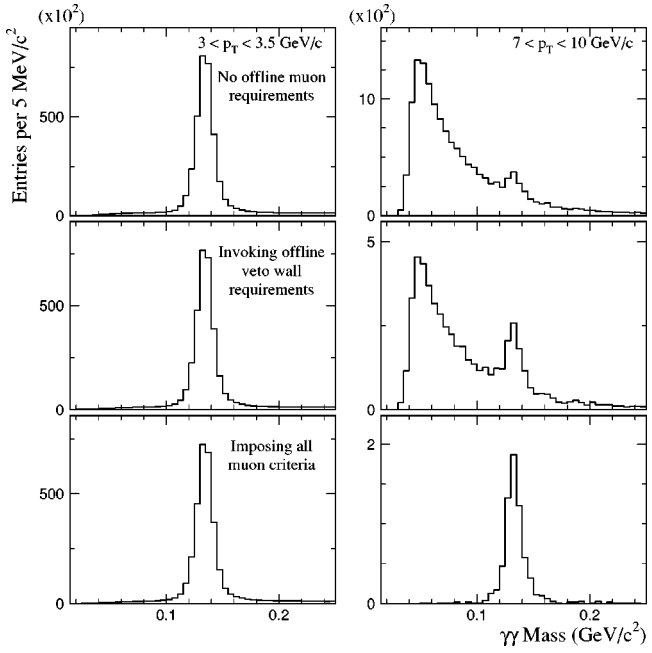

FIG. 5. Effect of muon rejection requirements on the invariant mass distribution in the π^0-mass region, for candidate $\gamma\gamma$ pairs with $3<p_T<3.5$ GeV/c (left) and $7<p_T<10$ GeV/c (right).

LOCAL⊗GLOBAL LO (1990 run) or SINGLE LOCAL LO (1991–1992 run), and SINGLE LOCAL HI. The transition points chosen between the lower and higher threshold triggers were determined by comparing the fully corrected results from each trigger, and were different for π^0 and η mesons, and also depended on rapidity. For $p_T>4.0$ GeV/c, the SINGLE LOCAL HI trigger was used exclusively for both π^0 and η mesons.

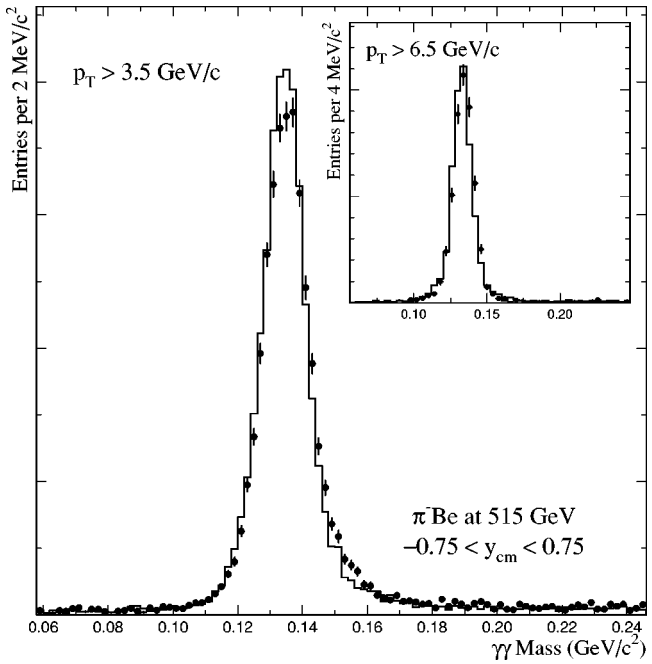

FIG. 6. Comparison between data (histogram) and the Monte Carlo (●) for $\gamma\gamma$ combinations in the π^0 mass region for two requirements on minimum p_T. The distributions have been normalized to unit area.

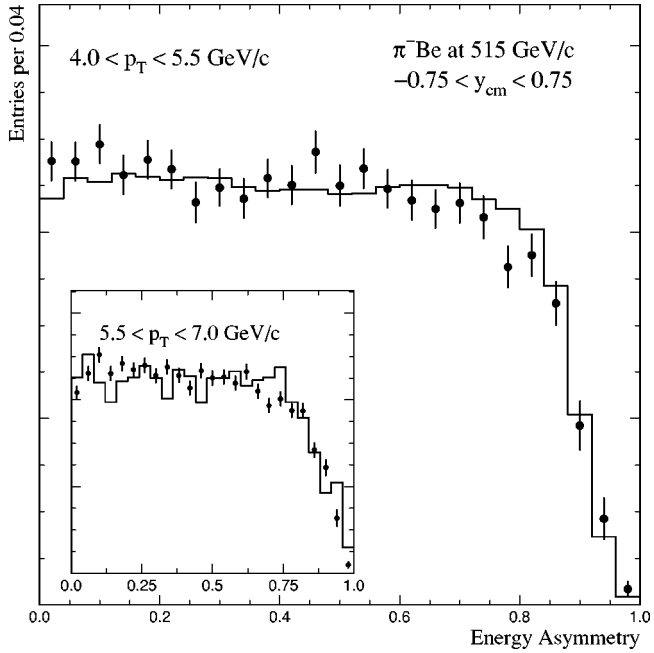

FIG. 7. Comparison of the background subtracted $\gamma\gamma$ energy asymmetry distribution in the π^0 signal region in the data (histogram) and Monte Carlo simulation (●). Shown are the comparisons for two p_T intervals, $4.0<p_T<5.5$ GeV/c and $5.5<p_T<7.0$ GeV/c. The distributions have been normalized to unit area.

D. Beam halo muon rejection

Spurious triggers were produced by muons in the beam halo that deposited energy in the electromagnetic calorimeter in random coincidence with an interaction in the target. Particularly in the outer regions of the EMLAC, such energy depositions can produce background at low $\gamma\gamma$ mass values due to the occasional splitting of the muon-induced showers into two closely separated photon candidates (see Fig. 5). The pretrigger logic used signals from the VW to reject events associated with such muons in the beam halo. The off-line analysis employed expanded requirements on the latched VW signals, and imposed requirements upon the direction of reconstructed showers, the shower shape, and the total p_T imbalance in the event to further reduce this background. The effects of these off-line rejection requirements on the $\gamma\gamma$ invariant mass distribution are shown in Fig. 5 for $\gamma\gamma$ pairs with $3<p_T<3.5$ GeV/c (left) and $7<p_T<10$ GeV/c (right). The rejection requirements completely eliminate the large muon-induced background in the high-p_T bin while having very little effect on the signal. A more detailed description of these requirements can be found in Ref. [16].

E. Detector simulation

The Meson West spectrometer was modeled via a detailed GEANT [31] simulation. A preprocessor was used to convert GEANT information into the hits and strip energies measured

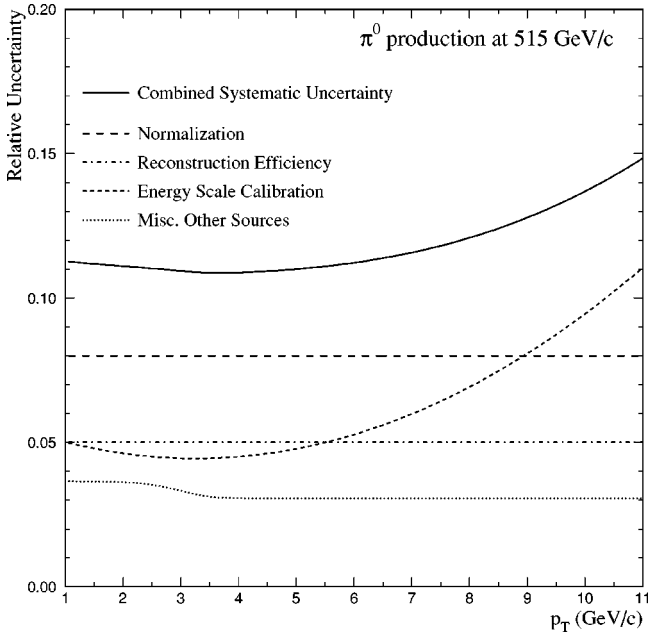

FIG. 8. Combined relative systematic uncertainty for π^0 production as a function of p_T (solid line). Also shown are the contributions from the various sources of systematic uncertainty.

by the various detectors. The preprocessor simulated hardware effects, such as channel noise and gain variations. Monte Carlo generated events were then processed through the same reconstruction software used to analyze the data. This accounted for inefficiencies and biases in the reconstruction algorithms. Reconstruction inefficiencies for π^0

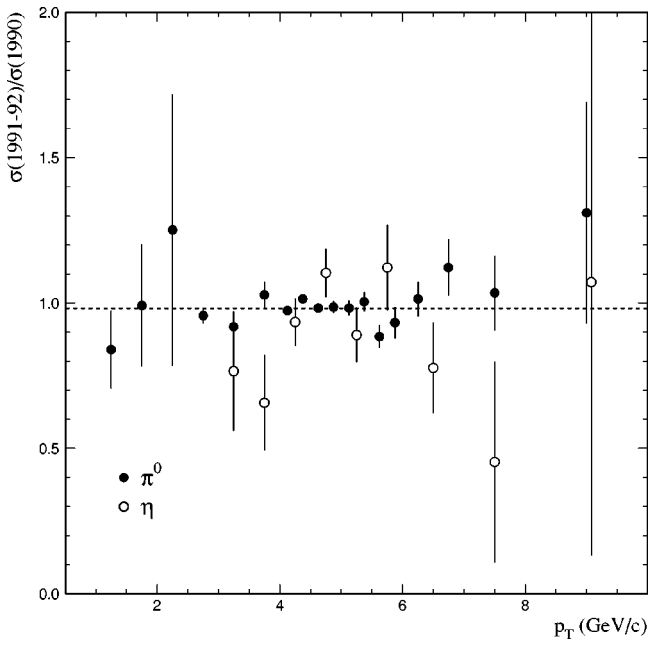

FIG. 9. Ratio of production cross sections by 515 GeV/c π^- beam on Be from the 1991–1992 fixed target run to those obtained from the 1990 run. The error bars reflect only statistical uncertainties for $p_T > 2.0$ GeV/c. The dashed line is a fit to the ratio of π^0 cross sections.

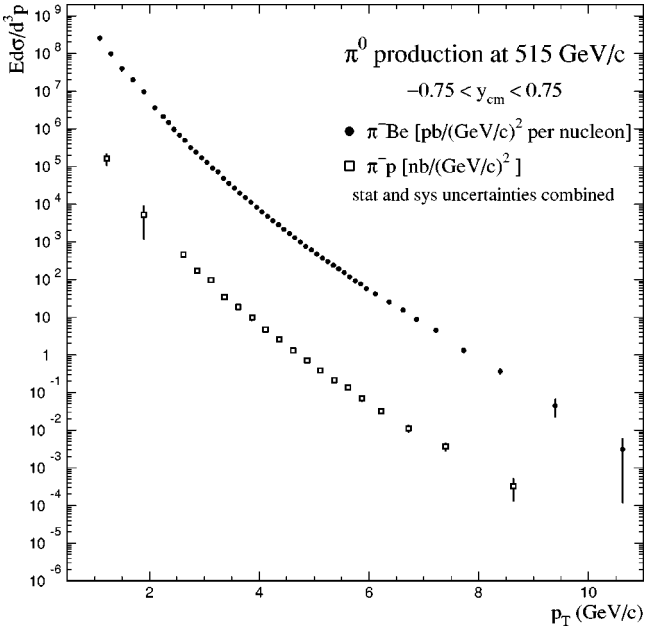

FIG. 10. Invariant differential cross sections (per nucleon) for π^0 production as a function of p_T in $\pi^- p$ and π^-Be interactions at 515 GeV/c. Cross sections have been averaged over the rapidity range, $-0.75 \leqslant y_{cm} \leqslant 0.75$. The error bars represent the combined statistical and systematic uncertainties.

and η mesons were relatively small over most of the kinematic range. More information on the detailed simulation of the Meson West spectrometer can be found in Ref. [16]. We employed single particle distributions, reconstructed data,

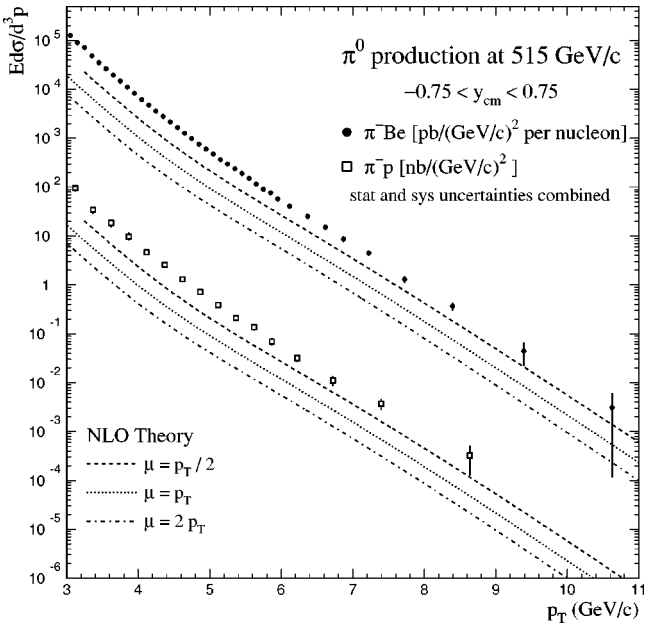

FIG. 11. Invariant differential cross sections (per nucleon) for π^0 production as a function of p_T in $\pi^- p$ and π^-Be interactions at 515 GeV/c. Cross sections have been averaged over the rapidity range, $-0.75 \leqslant y_{cm} \leqslant 0.75$. The error bars have statistical and systematic uncertainties added in quadrature. Overlayed on the data are NLO PQCD results.

TABLE I. Invariant differential cross section ($Ed\sigma/d^3p$) per nucleon for the inclusive reaction $\pi^-\mathrm{Be}\rightarrow\pi^0X$ at 515 GeV/c, averaged over the rapidity interval $-0.75\leqslant y_{\mathrm{cm}}\leqslant 0.75$.

p_T [GeV/c]	π^-Be at 515 GeV/c [μb/(GeV/c)^2]
1.00–1.20	258±36
1.20–1.40	98±14
1.40–1.60	39.9±6.0
1.60–1.80	20.0±2.6
1.80–2.00	9.6±1.3
2.00–2.20	3.68±0.36±0.43
2.20–2.30	2.134±0.054±0.25
2.30–2.40	1.475±0.038±0.17
	[nb/(GeV/c)^2]
2.40–2.50	964±27±112
2.50–2.60	680±17±78
2.60–2.70	501±14±58
2.70–2.80	318.6±9.7±36.4
2.80–2.90	246.2±7.3±28.1
2.90–3.00	171.9±4.3±19.5
3.00–3.10	128.8±3.3±14.5
3.10–3.20	91.6±2.6±10.3
3.20–3.30	72.8±1.9±8.2
3.30–3.40	48.8±1.3±5.5
3.40–3.50	35.7±1.0±4.0
3.50–3.60	26.80±0.66±3.0
3.60–3.70	19.93±0.50±2.2
3.70–3.80	15.02±0.36±1.7
3.80–3.90	11.26±0.30±1.2
3.90–4.00	8.37±0.11±0.92
4.00–4.10	6.283±0.040±0.69
4.10–4.20	4.818±0.034±0.53
4.20–4.30	3.640±0.027±0.40
4.30–4.40	2.853±0.023±0.31
4.40–4.50	2.188±0.019±0.24
4.50–4.60	1.671±0.015±0.18
4.60–4.70	1.289±0.013±0.14
	[pb/(GeV/c)^2]
4.70–4.80	1000±11±110
4.80–4.90	764.0±9.6±83.8
4.90–5.00	611.9±8.6±67.2
5.00–5.10	480.7±7.3±52.9
5.10–5.20	369.7±6.1±40.8
5.20–5.30	301.1±5.5±33.3
5.30–5.40	240.2±4.9±26.6
5.40–5.50	193.4±4.3±21.4
5.50–5.60	152.8±3.7±17.0
5.60–5.70	117.6±3.2±13.1
5.70–5.80	92.0±2.8±10.3
5.80–5.90	78.0±2.6±8.7
5.90–6.00	57.9±2.2±6.5
6.00–6.25	41.7±1.2±4.7
6.25–6.50	25.52±0.91±2.9
6.50–6.75	15.42±0.68±1.8
6.75–7.00	5.80±0.50±1.0
7.00–7.50	4.53±0.25±0.53
7.50–8.00	1.32±0.13±0.16
8.00–9.00	0.369±0.050±0.046
9.00–10.00	0.045±0.022±0.006
10.00–12.00	0.0031±0.0031±0.0005

and the HERWIG [32] physics generator as inputs to the GEANT simulations. HERWIG calculations of π^0 and η spectra were weighted in p_T and rapidity using our measured results in an iterative fashion so that the final corrections were based on the data distributions rather than on the output of the physics generator.

Spectral effects were particularly important to the calibration of the EMLAC's energy response [21]. The calibration of the energy response was based on the reconstructed masses of π^0 mesons in the $\gamma\gamma$ decay mode. The steeply falling π^0 p_T spectrum, combined with the calorimeter's resolution, results in a small offset ($\approx$1%) in the mean reconstructed photon energies. We accounted for this offset, and for potential biases in the calibration procedure, by calibrating the simulated EMLAC in the same manner as the real detector. We also employed the simulation to evaluate the mean correction (as a function of photon energy) for energy deposited in the material upstream of the EMLAC. The impacts of detector resolution on the energy scale calibration and on the π^0 and η production spectra were incorporated in the overall reconstruction efficiency corrections.

Figure 6 compares the $\gamma\gamma$ mass spectra in the π^0 mass region to the simulation for two different minimum p_T cutoffs. In addition to providing evidence that the Monte Carlo simulated the EMLAC resolution well, the agreement between the levels of combinatorial background also indicates that the Monte Carlo provided a reasonable simulation of the underlying event structure. Figure 7 shows a comparison between the Monte Carlo simulation and the data for the background subtracted $\gamma\gamma$ energy asymmetry in the π^0 signal region, for two p_T intervals. This figure illustrates that the simulation accurately describes the losses of very low-energy photons.

F. Normalization

Electronic scalers that counted signals from the beam hodoscope, interaction counters, and beam hole counters were used to evaluate the number of beam particles incident on the target. Other scalers logged the state of the trigger and of components of the data acquisition system. Information from these scalers was used to determine the number of beam particles that traversed the spectrometer when it was ready to record data. This number was corrected for multiple occupancy in the beam ($\approx$3%), the absorption of beam in the target material ($\approx$6% for the Be target and $\approx$3% for H_2), and for the μ^- content of the beam which was measured to be $\approx$0.5% [29].

The normalization of the low p_T π^0 cross section was independently verified using events from the prescaled beam and interaction trigger samples. In these samples, the absolute normalization is obtained simply by counting the recorded events selected by these triggers. For these low p_T events, the normalization as determined via the scalers and via event counting techniques agreed to 3% accuracy.

An analysis of negative secondary beam production by 800 GeV/c primary protons indicates a small ($\approx$1%) K^- component in the incident 515 GeV/c beam. The meson production cross sections were corrected for this K^- component

TABLE II. Invariant differential cross section ($Ed\sigma/d^3p$) for the inclusive reaction $\pi^- p \to \pi^0 X$ at 515 GeV/c, averaged over the rapidity interval $-0.75 \leqslant y_{\rm cm} \leqslant 0.75$.

p_T [GeV/c]	$\pi^- p$ at 515 GeV/c [μb/(GeV/c)^2]
1.00–1.50	163 ± 58
1.50–2.50	5.2 ± 4.1
	[nb/(GeV/c)^2]
2.50–2.75	$459 \pm 34 \pm 53$
2.75–3.00	$172 \pm 14 \pm 20$
3.00–3.25	$97.2 \pm 8.4 \pm 11.0$
3.25–3.50	$34.7 \pm 3.8 \pm 3.9$
3.50–3.75	$18.7 \pm 2.6 \pm 2.1$
3.75–4.00	$9.9 \pm 1.5 \pm 1.1$
4.00–4.25	$4.72 \pm 0.12 \pm 0.52$
4.25–4.50	$2.612 \pm 0.086 \pm 0.29$
4.50–4.75	$1.316 \pm 0.048 \pm 0.14$
	[pb/(GeV/c)^2]
4.75–5.00	$722 \pm 33 \pm 79$
5.00–5.25	$390 \pm 24 \pm 43$
5.25–5.50	$215 \pm 16 \pm 24$
5.50–5.75	$138 \pm 13 \pm 15$
5.75–6.00	$70.4 \pm 9.4 \pm 7.9$
6.00–6.50	$32.1 \pm 4.1 \pm 3.6$
6.50–7.00	$11.3 \pm 2.3 \pm 1.3$
7.00–8.00	$3.73 \pm 0.87 \pm 0.44$
8.00–10.00	$0.33 \pm 0.19 \pm 0.04$

under the assumption that meson production by a K^- beam is half that of a π^- beam [26,33].

G. Summary of systematic uncertainties

The principal contributions to the systematic uncertainty arose from the following sources: calibration of photon energy response, π^0 and η reconstruction efficiency and detector-resolution unsmearing, and overall normalization. The relative systematic uncertainty for π^0 production is shown as a function of p_T in Fig. 8. Included in the figure are curves showing the contributions from the major sources of systematic uncertainty. Other sources of uncertainty which contribute at the 1%–2% level include background subtraction, incident beam contamination, beam halo muon rejection, geometric acceptance, photon conversions, trigger response, and vertex finding. The total systematic uncertainty is calculated by combining in quadrature all the individual uncertainties. The uncertainties for η production are similar to those for π^0 production, except for the uncertainty in the trigger response, which is $\approx$5% at low p_T. The actual systematic uncertainties are quoted in the appropriate tables of cross sections, except at low p_T, where the statistical and systematic uncertainties have been combined because of the large correlation between them.

A cross-check of the systematics can be obtained by comparing the results for meson production from the 1991–1992 data sample to the results from the 1990 data sample for independent analyses. The ratio of the π^0 and η production cross sections from the 1991–1992 run to the 1990 run is shown in Fig. 9. A fit to the ratio of π^0 cross sections yields 0.982 ± 0.006, which is well within the systematic uncertainties described earlier in this section.

The secondary pion beam was determined to have a mean momentum of 515 ± 2 GeV/c with an estimated halfwidth of ≈ 30 GeV/c. This momentum spread introduces a small uncertainty ($\approx$5%) in comparisons of theory with data.

IV. RESULTS AND DISCUSSION

A. π^0 production

The inclusive π^0 cross sections per nucleon versus p_T are shown in Fig. 10 for 515 GeV/c π^- beam incident upon beryllium and liquid hydrogen targets. The statistical and systematic uncertainties are combined in quadrature [34]. Note that the cross section is in units of pb/(GeV/c)^2 per nucleon for the Be target and in nb/(GeV/c)^2 for the H_2 target. The measurements on beryllium were obtained using the combined statistics from the 1990 and 1991–1992 runs. Because of the steeply falling spectra, the data are plotted at abscissa values that correspond to the average values of the cross section in each p_T bin, assuming local exponential p_T dependence [35]. The cross sections are also tabulated in Tables I–IV.

In Fig. 11, the measured inclusive π^0 cross sections are compared to NLO PQCD results [3] using Glück-Reya-Vogt (GRV) [36] parton distributions, Kniehl-Kramer-Pötter (KKP) [37] fragmentation functions, and factorization scales of $\mu = p_T/2$, p_T, and $2p_T$ (the renormalization and fragmentation scales have been set equal to the value of the factorization scale). The PQCD calculations for the Be target were adjusted to account for nuclear effects using the HIJING Monte Carlo calculation [38]. The large scale dependence in the calculations is insufficient to raise the predicted cross sections up to the values indicated by the data.

These discrepancies have been interpreted [4–7] as arising from additional soft-gluon emission in the initial state that is not included in the NLO calculation, and which results in sizable parton k_T before the hard collision (for a different perspective, see the discussion in Ref. [9]). Soft-gluon (or k_T) effects are expected in all hard-scattering processes, such as the inclusive production of jets, high-p_T mesons, and direct photons [39–42]. The Collins-Soper-Sterman resummation formalism [43] provides a rigorous basis for understanding these radiative effects, and there have been several recent efforts to derive resummation descriptions for the inclusive direct-photon [44–48], jet [49], and dijet cross sections [50–52]. The calculation of Ref. [44] for inclusive direct-photon production, which includes the effects of soft-gluon resummation near the kinematic threshold limit ($x_T = 2p_T/\sqrt{s} \to 1$), has a far smaller sensitivity to scale, compared to NLO calculations, and provides cross sections close to those of NLO calculations with a scale of $\mu = p_T/2$. Also, for our

TABLE III. The averaged invariant differential cross section ($Ed\sigma/d^3p$) per nucleon as a function of rapidity and p_T for the inclusive reaction $\pi^-\mathrm{Be}\rightarrow\pi^0X$ at 515 GeV/c.

	p_T (GeV/c)			
y_{cm}	1.00–1.50 [μb/(GeV/c)^2]	1.50–2.00 [μb/(GeV/c)^2]	2.00–2.50 [μb/(GeV/c)^2]	2.50–3.00 [nb/(GeV/c)^2]
−0.750–−0.625	133±30	13.4±3.7	1.87±0.86±0.22	377±26±43
−0.625–−0.500				404±24±46
−0.500–−0.375	176±29	18.6±4.5	2.577±0.083±0.30	369±24±42
−0.375–−0.250				339±16±39
−0.250–−0.125	150±27	23.4±4.1	2.555±0.055±0.30	379±16±43
−0.125–0.000				408±15±47
0.000–0.125	173±31	19.8±4.0	2.554±0.045±0.30	414±14±47
0.125–0.250				396±12±45
0.250–0.375	126±22	24.9±4.5	2.430±0.049±0.28	397±12±46
0.375–0.500				357±12±41
0.500–0.625	146±24	15.0±3.2	2.267±0.052±0.27	371±13±43
0.625–0.750				337±12±39
	3.00–3.50 [nb/(GeV/c)^2]	3.50–4.00 [nb/(GeV/c)^2]	4.00–4.50 [nb/(GeV/c)^2]	4.50–5.00 [nb/(GeV/c)^2]
−0.750–−0.625	61.4±5.7±6.9	10.48±0.98±1.2	2.220±0.072±0.24	0.620±0.022±0.068
−0.625–−0.500	61.6±5.8±6.9	11.70±0.96±1.3	2.794±0.057±0.31	0.778±0.019±0.085
−0.500–−0.375	74.1±4.1±8.3	14.42±0.47±1.6	3.342±0.044±0.37	0.872±0.016±0.096
−0.375–−0.250	69.3±3.4±7.8	15.11±0.57±1.7	3.705±0.041±0.41	0.964±0.017±0.11
−0.250–−0.125	77.9±2.9±8.7	17.49±0.66±1.9	4.107±0.038±0.45	1.128±0.018±0.12
−0.125–0.000	84.1±2.4±9.4	18.74±0.53±2.1	4.607±0.040±0.51	1.241±0.018±0.14
0.000–0.125	87.5±1.7±9.8	18.32±0.54±2.0	4.580±0.037±0.50	1.257±0.018±0.14
0.125–0.250	85.5±1.7±9.6	18.76±0.61±2.1	4.571±0.038±0.50	1.230±0.017±0.13
0.250–0.375	85.3±1.7±9.6	18.82±0.61±2.1	4.720±0.040±0.52	1.275±0.018±0.14
0.375–0.500	82.6±1.9±9.3	17.71±0.63±2.0	4.576±0.041±0.50	1.254±0.019±0.14
0.500–0.625	78.8±1.8±8.8	18.71±0.58±2.1	4.305±0.041±0.47	1.171±0.019±0.13
0.625–0.750	70.8±1.8±8.0	15.11±0.51±1.7	3.858±0.040±0.42	1.015±0.018±0.11
	5.00–5.50 [pb/(GeV/c)^2]	5.50–6.50 [pb/(GeV/c)^2]	6.50–8.00 [pb/(GeV/c)^2]	8.00–10.00 [pb/(GeV/c)^2]
−0.750–−0.625	177.2±8.5±20	31.8±2.1±3.6	2.08±0.26±0.24	0.109±0.050±0.013
−0.625–−0.500	212.8±7.5±23	44.1±2.2±4.9		
−0.500–−0.375	253.5±8.2±28	52.1±2.3±5.8	4.46±0.35±0.52	0.039±0.024±0.005
−0.375–−0.250	306.5±9.0±34	65.3±2.6±7.3		
−0.250–−0.125	326.7±8.8±36	73.4±2.8±8.2	6.83±0.43±0.79	0.199±0.066±0.024
−0.125–0.000	356.0±9.0±39	75.8±2.8±8.5		
0.000–0.125	380.9±9.0±42	88.4±2.9±9.9	8.43±0.46±0.98	0.355±0.080±0.043
0.125–0.250	383.7±8.9±42	82.5±2.8±9.2		
0.250–0.375	387.7±9.2±43	83.2±2.8±9.3	7.40±0.46±0.86	0.393±0.093±0.048
0.375–0.500	375.0±9.6±41	71.9±2.9±8.1		
0.500–0.625	343.5±9.4±38	76.1±2.9±8.5	6.48±0.49±0.75	0.133±0.069±0.016
0.625–0.750	299.4±8.9±33	56.9±2.6±6.4		

energies, the calculations of Refs. [47], [48], which simultaneously treat threshold and recoil effects in direct-photon production, yield a substantially larger cross section than the NLO result. However, no such calculations are available for inclusive meson production. In their absence, we use a PQCD-based model that incorporates transverse kinematics of initial-state partons to study the consequences of additional k_T for high-p_T production processes.

Because the unmodified PQCD cross sections fall rapidly with increasing p_T, the net effect of the ''k_T smearing'' is to increase the expected yield. Modified parton kinematics have been implemented in a Monte Carlo calculation of the leading-order (LO) cross sections for high-p_T particle production [53], with the k_T distribution for each of the incom-

TABLE IV. The averaged invariant differential cross section ($Ed\sigma/d^3p$) as a function of rapidity and p_T for the inclusive reaction $\pi^- p \to \pi^0 X$ at 515 GeV/c.

	p_T (GeV/c)			
y_{cm}	2.50–3.00 [nb/(GeV/c)^2]	3.00–3.50 [nb/(GeV/c)^2]	3.50–4.00 [nb/(GeV/c)^2]	4.00–4.50 [nb/(GeV/c)^2]
−0.750–−0.625	291±71±33	51±15±5.7	5.5±3.7±0.6	1.97±0.29±0.22
−0.625–−0.500				2.95±0.34±0.32
−0.500–−0.375	300±62±34	50.6±9.4±5.7	3.9±2.9±0.4	3.59±0.34±0.39
−0.375–−0.250				3.83±0.28±0.42
−0.250–−0.125	294±32±34	77±12±8.6	16.1±3.0±1.8	3.60±0.29±0.40
−0.125–0.000				3.89±0.21±0.43
0.000–0.125	349±31±40	76±10±8.6	22.7±4.0±2.5	4.64±0.23±0.51
0.125–0.250				4.08±0.21±0.45
0.250–0.375	371±25±42	67.9±9.2±7.6	20.8±3.3±2.3	4.23±0.20±0.47
0.375–0.500				4.00±0.22±0.44
0.500–0.625	289±27±33	73±11±8.2	16.8±4.6±1.9	3.90±0.25±0.43
0.625–0.7503.				32±0.24±0.37
	4.50–5.00 [nb/(GeV/c)^2]	5.00–5.50 [pb/(GeV/c)^2]	5.50–6.50 [pb/(GeV/c)^2]	6.50–8.00 [pb/(GeV/c)^2]
−0.750–−0.625	0.493±0.091±0.054	119±30±13	45±15±5.1	3.2±1.9±0.4
−0.625–−0.500	0.68±0.11±0.07	262±67±29	69±18±7.7	
−0.500–−0.375	0.90±0.10±0.10	320±54±35	76±17±8.5	2.2±1.3±0.3
−0.375–−0.250	0.901±0.095±0.099	277±45±31	71±17±7.9	
−0.250–−0.125	1.127±0.096±0.12	366±50±40	61±14±6.9	7.5±2.5±0.9
−0.125–−0.000	1.16±0.10±0.13	408±55±45	62±13±6.9	
0.000–0.125	1.116±0.095±0.12	325±46±36	89±16±9.9	9.3±2.7±1.1
0.125–0.250	1.44±0.11±0.16	341±48±38	69±14±7.7	
0.250–0.375	1.287±0.100±0.14	380±50±42	103±18±12	7.6±2.5±0.9
0.375–0.500	1.104±0.099±0.12	360±51±40	59±15±6.6	
0.500–0.625	1.09±0.11±0.12	253±47±28	57±14±6.4	7.7±2.7±0.9
0.625–0.750	0.93±0.11±0.10	223±46±25	58±16±6.5	

ing partons represented by a Gaussian with one adjustable parameter ($\langle k_T \rangle$). Unfortunately, no such program is available for NLO calculations, and so we approximate the effect of k_T smearing by multiplying the NLO cross sections by the corresponding LO k_T-enhancement factors. Admittedly, this procedure involves a risk of double counting since some of the k_T enhancement may already be contained in the NLO calculation. However, we expect such double-counting effects to be small.

In the calculation of the LO k_T-enhancement factors we employ $\langle k_T \rangle$ values representative of those found from comparisons of kinematic distributions in data involving production of high-mass $\gamma\gamma$, $\gamma\pi^0$, and $\pi^0\pi^0$ systems with calculations relying on the same LO program (see Refs. [4–6] for further details). For these comparisons, we used the LO versions of the GRV parton distributions and (where appropriate) KKP fragmentation functions, and an average transverse momentum of 0.6 GeV/c for the π^0 mesons relative to the fragmenting parton direction (varying this parameter in the range 0.3–0.7 GeV/c does not affect our conclusions) [54,55].

Comparisons of the k_T-enhanced calculations with data at 515 GeV/c are displayed in Fig. 12, indicating good agreement for this $\langle k_T \rangle$ value for points with $p_T \gtrsim 4$ GeV/c. Figure 13 shows the π^-Be cross sections at 515 GeV/c versus rapidity for several intervals in p_T. The shapes and normalizations of the data are in reasonable agreement with the k_T-enhanced calculations for $p_T \gtrsim 4$ GeV/c.

In a previous publication [16], this experiment reported results for π^0 production in pp and pBe interactions at 800 and 530 GeV/c. This offers the opportunity to compare production cross sections by incident π^- and p beams. In Fig. 14, the ratio of invariant cross sections for π^0 production by 515 GeV/c π^- and 800 GeV/c p beams is shown as a function of x_T (comparing results at approximately the same incident momentum per valence quark). Both theoretical and experimental uncertainties are reduced in a ratio allowing, in principle, a more sensitive test of the calculations. In this figure, the data are compared to conventional ($\langle k_T \rangle = 0$) and k_T-enhanced NLO results using KKP fragmentation functions. The k_T-enhanced theory accommodates the data better than the conventional theory.

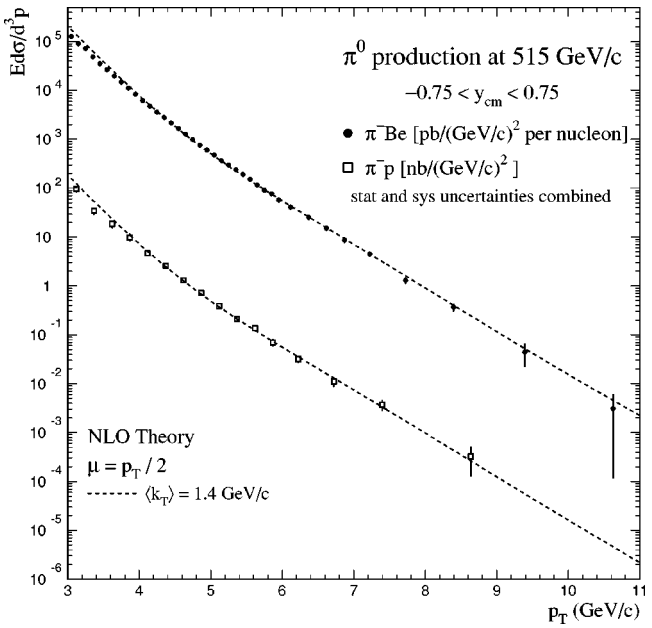

FIG. 12. Invariant differential cross sections (per nucleon) for π^0 production as a function of p_T in $\pi^- p$ and π^-Be interactions at 515 GeV/c. Cross sections have been averaged over the rapidity range, $-0.75 \leqslant y_{\rm cm} \leqslant 0.75$. The error bars have statistical and systematic uncertainties added in quadrature. The curves represent the k_T-enhanced NLO QCD calculations for $\langle k_T \rangle = 1.4$ GeV/c.

B. η production

Cross sections for inclusive η production are tabulated in Tables V–VIII. Theoretical descriptions of η-meson production differ from the π^0 case primarily because of differences in the fragmentation of partons into the particles of interest. To investigate this effect, we present η/π^0 relative production rates as functions of p_T and $y_{\rm cm}$ (for two p_T ranges) in

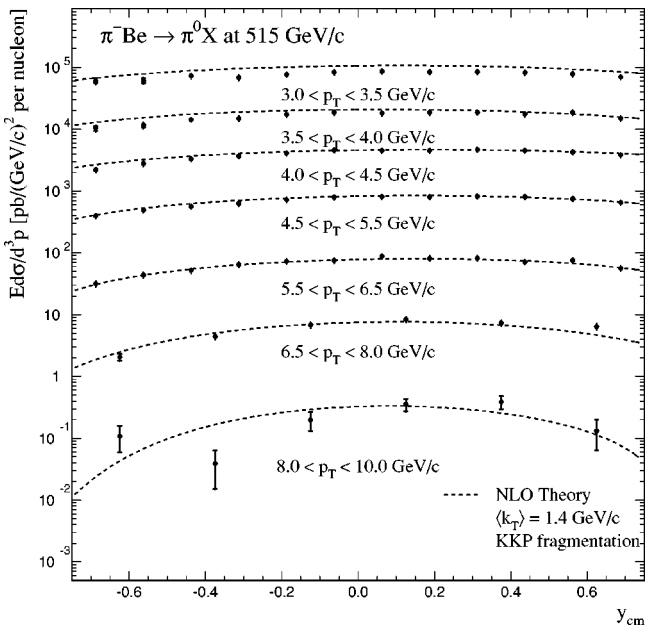

FIG. 13. Invariant cross sections per nucleon for π^0 production in π^-Be interactions at 515 GeV/c. Cross sections are shown versus $y_{\rm cm}$ for several intervals in p_T. The curves represent k_T-enhanced NLO QCD calculations for $\langle k_T \rangle = 1.4$ GeV/c. The error bars have statistical and systematic uncertainties added in quadrature.

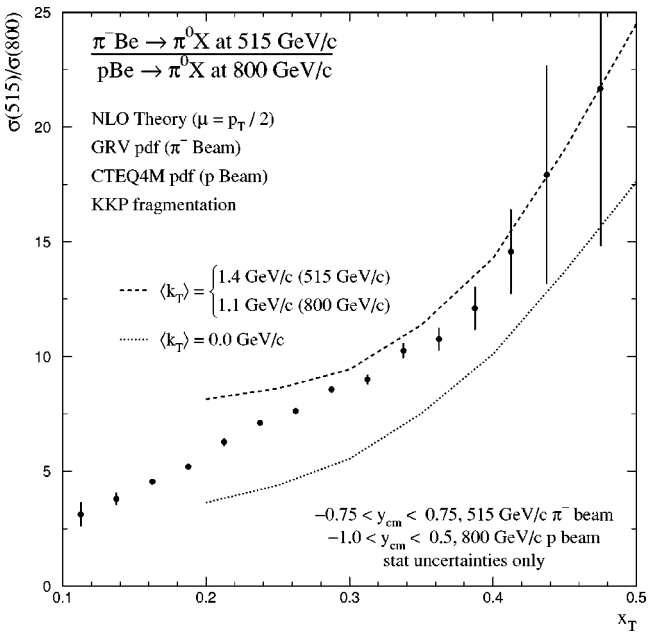

FIG. 14. Ratio of 515 GeV/c π^- to 800 GeV/c p beam π^0 production cross sections as a function of x_T, compared to conventional and k_T-enhanced NLO QCD results.

TABLE V. Invariant differential cross section ($Ed\sigma/d^3p$) per nucleon for the inclusive reaction π^-Be$\rightarrow \eta X$ at 515 GeV/c, averaged over the rapidity interval $-0.75 \leqslant y_{\rm cm} \leqslant 0.75$.

p_T [GeV/c]	π^-Be at 515 GeV/c [nb/(GeV/c)^2]
3.00–3.20	$55.1 \pm 7.6 \pm 7.0$
3.20–3.40	$24.0 \pm 4.0 \pm 3.0$
3.40–3.60	$17.1 \pm 2.1 \pm 2.1$
3.60–3.80	$7.99 \pm 0.98 \pm 0.95$
3.80–4.00	$4.47 \pm 0.21 \pm 0.52$
4.00–4.20	$2.464 \pm 0.099 \pm 0.29$
4.20–4.40	$1.521 \pm 0.062 \pm 0.18$
	[pb/(GeV/c)^2]
4.40–4.60	$931 \pm 41 \pm 108$
4.60–4.80	$577 \pm 25 \pm 67$
4.80–5.00	$356 \pm 16 \pm 41$
5.00–5.25	$194.8 \pm 9.6 \pm 22.7$
5.25–5.50	$111.5 \pm 6.4 \pm 13.0$
5.50–5.75	$70.0 \pm 4.8 \pm 8.2$
5.75–6.00	$33.8 \pm 3.1 \pm 4.0$
6.00–6.50	$20.3 \pm 1.5 \pm 2.4$
6.50–7.00	$6.30 \pm 0.73 \pm 0.76$
7.00–8.00	$1.23 \pm 0.22 \pm 0.15$
8.00–9.00	$0.227 \pm 0.084 \pm 0.029$
9.00–10.00	$0.035 \pm 0.040 \pm 0.005$

TABLE VI. Invariant differential cross section ($Ed\sigma/d^3p$) for the inclusive reaction $\pi^- p \to \eta X$ at 515 GeV/c, averaged over the rapidity interval $-0.75 \leqslant y_{\rm cm} \leqslant 0.75$.

p_T [GeV/c]	$\pi^- p$ at 515 GeV/c [nb/(GeV/c)^2]
3.00–3.50	$70 \pm 63 \pm 9$
3.50–4.00	$9.2 \pm 3.9 \pm 1.1$
4.00–4.50	$1.78 \pm 0.31 \pm 0.21$
	[pb/(GeV/c)^2]
4.50–5.00	$400 \pm 110 \pm 50$
5.00–5.50	$123 \pm 31 \pm 14$
5.50–6.00	$19 \pm 18 \pm 2$
6.00–7.00	$7.9 \pm 4.7 \pm 0.9$
7.00–8.00	$0.37 \pm 0.98 \pm 0.05$

Fig. 15. Also shown are predictions for the ratios from the PYTHIA [56] and HERWIG [57] Monte Carlo event generators. The ratios from HERWIG are much smaller than both our measurements and the results from PYTHIA.

TABLE VIII. The averaged invariant differential cross section ($Ed\sigma/d^3p$) as a function of rapidity and p_T for the inclusive reaction $\pi^- p \to \eta X$ at 515 GeV/c. Units are pb/(GeV/c)^2.

	p_T (GeV/c)	
$y_{\rm cm}$	4.00–5.00	5.00–6.00
-0.75–-0.50	$560 \pm 550 \pm 64$	—
-0.50–-0.25	$960 \pm 460 \pm 110$	$75 \pm 43 \pm 8.7$
-0.25–0.00	$1180 \pm 360 \pm 140$	$39 \pm 39 \pm 4.6$
0.00–0.25	$1860 \pm 430 \pm 220$	$149 \pm 47 \pm 17$
0.25–0.50	$1030 \pm 270 \pm 120$	$155 \pm 50 \pm 18$
0.50–0.75	$970 \pm 220 \pm 110$	$44 \pm 43 \pm 5.1$

V. SUMMARY

The invariant cross sections for π^0 and η production have been measured for $\pi^- p$ and π^-Be collisions at 515 GeV/c as functions of p_T and $y_{\rm cm}$ over the kinematic range $1 < p_T < 11$ GeV/c and $-0.75 \leqslant y_{\rm cm} \leqslant 0.75$. The measured inclusive π^0 cross sections are larger than the results of NLO PQCD calculations, but agree with k_T-enhanced calculations for $p_T \gtrsim 4$ GeV/c. The measured η/π^0 production ratios, which

TABLE VII. The averaged invariant differential cross section ($Ed\sigma/d^3p$) per nucleon as a function of rapidity and p_T for the inclusive reaction π^-Be$\to \eta X$ at 515 GeV/c. Units are pb/(GeV/c)^2.

$y_{\rm cm}$	p_T (GeV/c)		
	3.00–4.00	4.00–4.50	4.50–5.00
-0.750–-0.625	$14200 \pm 6300 \pm 1700$	$690 \pm 260 \pm 80$	$290 \pm 89 \pm 34$
-0.625–-0.500		$890 \pm 230 \pm 100$	$281 \pm 62 \pm 33$
-0.500–-0.375	$17100 \pm 5700 \pm 2100$	$1310 \pm 180 \pm 150$	$342 \pm 52 \pm 40$
-0.375–-0.250		$1830 \pm 180 \pm 210$	$461 \pm 45 \pm 53$
-0.250–-0.125	$27400 \pm 4600 \pm 3400$	$1730 \pm 150 \pm 200$	$586 \pm 53 \pm 68$
-0.125–0.000		$2230 \pm 140 \pm 260$	$562 \pm 47 \pm 65$
0.000–0.125	$27800 \pm 2300 \pm 3400$	$1770 \pm 130 \pm 210$	$584 \pm 47 \pm 68$
0.125–0.250		$2430 \pm 140 \pm 280$	$657 \pm 55 \pm 76$
0.250–0.375	$23900 \pm 2500 \pm 2900$	$2390 \pm 150 \pm 280$	$689 \pm 52 \pm 80$
0.375–0.500		$2300 \pm 140 \pm 270$	$695 \pm 51 \pm 80$
0.500–0.625	$18300 \pm 2200 \pm 2200$	$2050 \pm 120 \pm 240$	$656 \pm 47 \pm 76$
0.625–0.750		$2090 \pm 120 \pm 240$	$601 \pm 44 \pm 70$
	5.00–5.50	5.50–6.50	6.50–8.00
-0.750–-0.625	$37 \pm 15 \pm 4.3$	$6.9 \pm 4.6 \pm 0.8$	$0.49 \pm 0.49 \pm 0.06$
-0.625–-0.500	$79 \pm 22 \pm 9.2$	$23.1 \pm 4.9 \pm 2.7$	
-0.500–-0.375	$142 \pm 22 \pm 17$	$18.7 \pm 4.3 \pm 2.2$	$1.32 \pm 0.48 \pm 0.16$
-0.375–-0.250	$126 \pm 17 \pm 15$	$32.5 \pm 5.7 \pm 3.8$	
-0.250–-0.125	$158 \pm 17 \pm 18$	$36.9 \pm 4.5 \pm 4.3$	$3.66 \pm 0.72 \pm 0.45$
-0.125–0.000	$145 \pm 20 \pm 17$	$43.0 \pm 5.6 \pm 5.1$	
0.000–0.125	$139 \pm 19 \pm 16$	$33.7 \pm 5.3 \pm 4.0$	$3.60 \pm 0.78 \pm 0.44$
0.125–0.250	$199 \pm 22 \pm 23$	$46.0 \pm 5.5 \pm 5.4$	
0.250–0.375	$227 \pm 22 \pm 26$	$48.4 \pm 5.4 \pm 5.7$	$4.41 \pm 0.86 \pm 0.54$
0.375–0.500	$220 \pm 22 \pm 26$	$46.4 \pm 6.5 \pm 5.5$	
0.500–0.625	$186 \pm 21 \pm 22$	$41.9 \pm 5.9 \pm 4.9$	$3.90 \pm 0.78 \pm 0.47$
0.625–0.750	$174 \pm 18 \pm 20$	$36.2 \pm 5.2 \pm 4.3$	

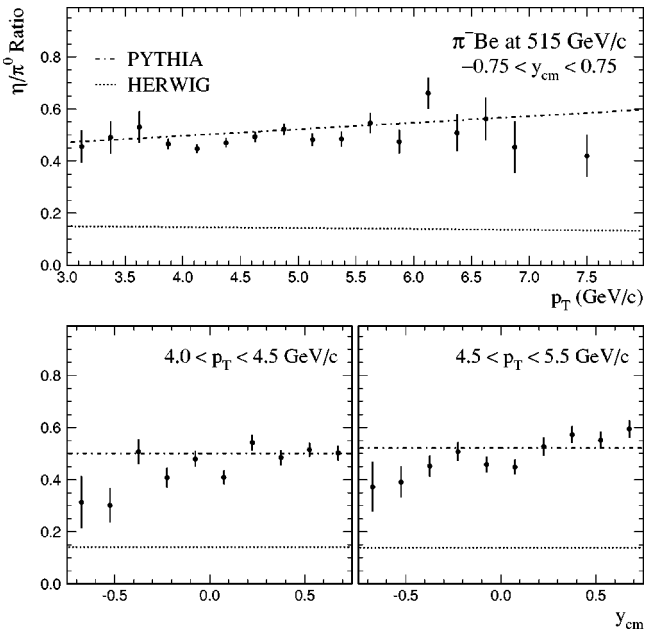

FIG. 15. Ratios of η to π^0 invariant cross sections at 515 GeV/c as functions of p_T (top) and of $y_{\rm cm}$ (bottom) for two p_T ranges. The error bars reflect only the statistical uncertainties. Also shown are predictions for η/π^0 from PYTHIA and HERWIG.

provide information about the relative fragmentation of partons into these mesons, agree fairly well with expectations from PYTHIA, but not with those from HERWIG.

ACKNOWLEDGMENTS

We thank the U.S. Department of Energy, the National Science Foundation, including its Office of International Programs, and the Universities Grants Commission of India, for their support of this research. The staff and management of Fermilab are thanked for their efforts in making available the beam and computing facilities that made this work possible. We are also pleased to acknowledge the contributions of our colleagues on Fermilab experiment E672. We acknowledge the contributions of the following colleagues for their help in the operation and upgrade of the Meson West spectrometer: W. Dickerson, E. Pothier from Northeastern University; J. T. Anderson, E. Barsotti, Jr., H. Koecher, P. Madsen, D. Petravick, R. Tokarek, J. Tweed, D. Allspach, J. Urbin, and the cryo crews from Fermi National Accelerator Laboratory; T. Haelen, C. Benson, L. Kuntz, and D. Ruggiero from the University of Rochester; the technical staffs of Michigan State University and Pennsylvania State University for the construction of the straw tubes and of the University of Pittsburgh for the silicon detectors. We would also like to thank the following commissioning run collaborators for their invaluable contributions to the hardware and software infrastructure of the original Meson West spectrometer: G. Alverson, G. Ballocchi, R. Benson, D. Berg, D. Brown, D. Carey, T. Chand, C. Chandlee, S. Easo, W. Faissler, G. Glass, I. Kourbanis, A. Lanaro, C. Nelson, Jr., D. Orris, B. Rajaram, K. Ruddick, A. Sinanidis, and G. Wu. We thank S. Catani, J. Ph. Guillet, B. Kniehl, J. Owens, G. Sterman, W. Vogelsang, and X.-N. Wang for many helpful discussions and for providing us with their QCD calculations.

[1] W. M. Geist *et al.*, Phys. Rep. **197**, 263 (1990).
[2] N. A. McCubbin, Rep. Prog. Phys. **44**, 65 (1981).
[3] F. Aversa *et al.*, Nucl. Phys. **B327**, 105 (1989).
[4] L. Apanasevich *et al.*, Phys. Rev. Lett. **81**, 2642 (1998).
[5] L. Apanasevich *et al.*, Phys. Rev. D **59**, 074007 (1999).
[6] L. Apanasevich *et al.*, Phys. Rev. D **63**, 014009 (2001).
[7] J. Huston *et al.*, Phys. Rev. D **51**, 6139 (1995).
[8] P. Aurenche *et al.*, Eur. Phys. J. C **9**, 107 (1999).
[9] P. Aurenche *et al.*, Eur. Phys. J. C **13**, 347 (2000).
[10] k_T denotes the magnitude of the effective transverse momentum vector, $\vec{k}_T$, of each of the two colliding partons.
[11] J. Breitweg *et al.*, Phys. Lett. B **472**, 175 (2000).
[12] J. Breitweg *et al.*, Phys. Lett. **511B**, 19 (2001).
[13] M. Fontannaz, J. P. Guillet, and G. Heinrich, Eur. Phys. J. C **21**, 303 (2001).
[14] M. Fontannaz, J. P. Guillet, and G. Heinrich, Eur. Phys. J. C **22**, 303 (2001).
[15] A. Zembrzuski and M. Krawczyk, Phys. Rev. D **64**, 114017 (2001).
[16] L. Apanasevich *et al.*, Phys. Rev. D **68**, 052001 (2003). During preparation of the current article, a computational error in correcting the measured cross sections for contributions due to minority particles in secondary beams was discovered. This error also affected the cross sections for π^0 and η production by 530 GeV/c protons. As a result, the cross section values in the tables for 530 GeV/c protons in the publication referenced here should be increased by 3.4%, a change that falls well within the total systematic uncertainties quoted therein.
[17] L. Apanasevich *et al.*, Report No. FERMILAB-Pub-00/054-E, hep-ex/0004012.
[18] L. Apanasevich *et al.*, Phys. Rev. D **56**, 1391 (1997).
[19] The figure does not include the Cherenkov detector, steel absorber, and the veto walls located upstream of the detector elements shown. The figure also excludes the muon identification system, which was located downstream of the detector elements shown in the diagram, and which was used primarily by Fermilab E672 to select events containing high mass dimuons.
[20] D. Allspach *et al.*, in *Advances in Cyrogenic Engineering*, edited by R. W. Fast (Plenum Press, New York, 1991), Vol. 37, p. 1495.
[21] L. Apanasevich *et al.*, Nucl. Instrum. Methods Phys. Res. A **417**, 50 (1998).
[22] R. Jesik *et al.*, Phys. Rev. Lett. **74**, 495 (1995).
[23] A. Gribushin *et al.*, Phys. Rev. D **53**, 4723 (1996).
[24] V. Koreshev *et al.*, Phys. Rev. Lett. **77**, 4294 (1996).
[25] A. Gribushin *et al.*, Phys. Rev. D **62**, 012001 (2000).
[26] D. Striley, Ph.D. thesis, University of Missouri at Columbia, 1996.
[27] I. Kourbanis, Ph.D. thesis, Northeastern University, 1989.
[28] L. Sorrell, ''The E706 Trigger System,'' E706 Note No. 201, 1994 (unpublished); Ph.D. thesis, Michigan State University, 1995.

[29] G. Osborne, Ph.D. thesis, University of Rochester, 1996.
[30] Particle Data Group, D. E. Groom *et al.*, Eur. Phys. J. C **15**, 1 (2000).
[31] F. Carminati *et al.*, computer code GEANT: Detector Description and Simulation Tool, CERN Program Library Long Writeup W5013, 1993.
[32] G. Marchesini *et al.*, Comput. Phys. Commun. **67**, 465 (1992), computer code HERWIG v5.6.
[33] G. Donaldson *et al.*, Phys. Rev. Lett. **40**, 917 (1978).
[34] At low p_T, where a fitting procedure was used to determine the signal, the statistical and systematic uncertainties due to the fit are highly correlated. This contribution to the uncertainty was calculated from the spread of points obtained from several independent fits. The other systematic uncertainties were then added in quadrature to obtain the total uncertainty.
[35] G. D. Lafferty and T. R. Wyatt, Nucl. Instrum. Methods Phys. Res. A **355**, 541 (1995).
[36] M. Glück, E. Reya, and A. Vogt, Z. Phys. C **63**, 127 (1992).
[37] B. A. Kniehl, G. Kramer, and B. Pötter, Nucl. Phys. **B582**, 514 (2000).
[38] X.-N. Wang, Nucl. Phys. **A661**, 609 (1999); X.-N. Wang (private communication regarding the use of this program with this incident beam). The calculation has not been tuned for pion beams and required a 10% shift in normalization to bring it into agreement with our result for π^0 production on Be relative to H_2.
[39] R. P. Feynman, R. D. Field, and G. C. Fox, Phys. Rev. D **18**, 3320 (1978).
[40] M. Fontannaz and D. Schiff, Nucl. Phys. **B132**, 457 (1978).
[41] A. P. Contogouris *et al.*, Nucl. Phys. **B179**, 461 (1981).
[42] A. P. Contogouris *et al.*, Phys. Rev. D **32**, 1134 (1985).
[43] J. Collins and D. Soper, Nucl. Phys. **B193**, 381 (1981); **B213**, 545(E) (1983); J. Collins, D. Soper, and G. Sterman, Phys. Lett. **109B**, 388 (1982).
[44] S. Catani *et al.*, J. High Energy Phys. **03**, 025 (1999).
[45] S. Catani, M. L. Mangano, and P. Nason, J. High Energy Phys. **07**, 024 (1998).
[46] H.-L. Lai and H.-N. Li, Phys. Rev. D **58**, 114020 (1998).
[47] E. Laenen, G. Sterman, and W. Vogelsang, Phys. Rev. Lett. **84**, 4296 (2000).
[48] C. E. Fink, hep-ph/0105276.
[49] N. Kidonakis and J. F. Owens, Phys. Rev. D **63**, 054019 (2001).
[50] E. Laenen, G. Oderda, and G. Sterman, Phys. Lett. B **438**, 173 (1998).
[51] N. Kidonakis, G. Oderda, and G. Sterman, hep-ph/9805279; in Proceedings of DIS98, 1998.
[52] N. Kidonakis, G. Oderda, and G. Sterman, Nucl. Phys. **B525**, 299 (1998).
[53] J. F. Owens, Rev. Mod. Phys. **59**, 465 (1987).
[54] A. G. Clark *et al.*, Nucl. Phys. **B160**, 397 (1979).
[55] A. L. S. Angelis *et al.*, Phys. Lett. **97B**, 163 (1980).
[56] T. Sjöstrand *et al.*, Comput. Phys. Commun. **135**, 238 (2001), computer code PYTHIA v6.220.
[57] G. Marchesini *et al.*, Comput. Phys. Commun. **67**, 465 (1992); G. Corcella *et al.*, J. High Energy Phys. **01**, 010 (2001), computer code HERWIG v6.5.